

# Intrinsic defects formation and subsequent direct and indirect transitions due to ammonia in rGO – ZnO nanocomposites

A. S. Bhattacharyya\*, Ritambhara Dash

Department of Metallurgical and Materials Engineering, Central University of Jharkhand, India

\*Corresponding author: E-mail: 2006asb@gmail.com; arnab.bhattacharya@cuja.ac.in

DOI: 10.5185/amp.2023.6186.1007

The rGO-ZnO composite was found promising improvement over the photocatalytic ability of pure ZnO and is useful for other Opto-chemical applications. ZnO/rGO composite was synthesized by the sol-gel method. The morphology of rGO caused better dispersion of the ZnO crystallites. The reducing agent ammonia was varied in concentration during the synthesis. A reduction in the crystallization was observed for lower concentrations (0 – 1%) of ammonia which got stabilized in higher concentrations (>1%). The crystalline morphology showed variations from being close to amorphous to 38 nm. The average crystallite size was 15 nm. The rGO induced nonradiative phononic modes in the optical transition process when present in lower concentration but interestingly aided the crystallization process in a preferential crystallographic orientation which however got lowered in intensity for >2% ammonia concentration. The defect states formed in the rGO/ZnO composite in the form of oxygen vacancies, zinc interstitials, and vacancies caused a decrease in band gap due to indirect transitions. The role of ammonia in the performance of the composites was found to be significant.

## Introduction

Zinc Oxide (ZnO) has properties of high refractive index, high binding energy, high thermal conductivity, good biocompatibility, and antibacterial and UV protection. It has numerous applications in electronic devices, photocatalysis, gas sensing, biomedical, skin treatment, filter in cigarettes, and biometric membranes [1-3]. ZnO is an n-type semiconductor with a band gap of 3.3 – 3.4 eV and exciton binding energy of 60 meV, transparent in the visible region, and a less toxic material. ZnO has preferential cytotoxicity against cancer cells which kills cancerous cells without affecting normal cells. The requirement of UV light in the photocatalytic application of ZnO has been reported to get nullified on metal ion doping [4,5].

Graphene oxide (GO) due to its morphology provides a larger surface area for efficient dispersion of metal oxide nanoparticles avoiding agglomeration. GO and reduced GO (r-GO) are helpful for photothermal catalysis, dye and contaminant adsorption, and catalytic esterification, and have been employed as catalyst supports due to their good adsorption performance, high stability, and high surface area [6-9].

ZnO/rGO composites have been reported to have many applications like anticorrosion, gas sensing, photocatalytic (with H<sub>2</sub> production), esterification of acetic acid, heterogeneous catalysis for the synthesis of various 3-substituted indoles in water and anti-cancer. The enhanced charge transport phenomena in rGO/ZnO have also been utilized in photodetection and heterojunction solar cells [10-19].

ZnO nanoparticles have been prepared by various physical and chemical methods [20-28]. Sol-gel techniques are one of the easiest techniques for the synthesis of ZnO with the possibility of doping or other alterations tuning the properties. In addition to the benefit of low cost, the sol-gel process has also the advantage of precise composition control of films making it suitable to examine material properties dominated by composition [29]. In this work, we have synthesized rGO/ ZnO composites by the Sol-gel method (being simple and easily tunable) and analyzed the effect of increasing the rGO percentage by increasing the concentration of the reducing agent ammonia (NH<sub>3</sub>) during synthesis. Ammonia is preferred over other gases for doping purposes due to its high chemical reactivity.

## Experimental methods

Zinc oxide nanoparticles were synthesized through the sol-gel method using zinc nitrate as a precursor. 5.9513 g of zinc nitrate with 40 ml of water is prepared and added with 1.0048 g of urea. The sample was kept for stirring for 3 hr. with a temperature of 120°C. As a result, ZnO is formed and transferred to a Petry dish. Calcination was done in an oven for 10 hr. at 100°C temperature. 0.1 g of prepared ZnO is taken with 20 ml of distilled water to prepare the ZnO solution.

Reduced Graphene oxide (rGO) was synthesized by using the well-known modified Hummers method. The graphite flakes (2 g) and NaNO<sub>3</sub> (1 g) were mechanically mixed, and transferred into concentrated H<sub>2</sub>SO<sub>4</sub>. KMnO<sub>4</sub> (6 g) was slowly added to the resultant solution under vigorous stirring. About 20 ml rGO in liquid solution form is taken. Both the solutions underwent ultrasonication for 30 min. The solutions were mixed and stirred for 1 hour by adding ammonia solution dropwise. Ammonia (NH<sub>3</sub>.H<sub>2</sub>O) acts as a reducing agent. Four (4) samples were prepared with 1ml, 2ml, 3ml and 4ml ammonia or 1%, 2%, 3% and 4%. All four samples were washed five times to maintain the sample pH of 7. Calcination was done for 10 hrs. The respective weights of samples obtained after drying were 0.0640 g, 0.0780 g, 0.0650 g, and 0.0683 g. The characterizations were done using XRD (Proto A-XRD with Cu K $\alpha$  = 1.54Å), UV-Vis spectrometer (UV 3600 Plus, Shimadzu, Japan and Photoluminescence spectrometer (Fluoromax-4, Horiba Scientific, USA).

## Results and discussions

Composites of ZnO and rGO by different ammonia concentrations (1-4%) were synthesized. Ammonia being the reducing agent of GO, shall cause a higher concentration of rGO upon increasing its concentration. The XRD spectra of synthesized compounds are shown in **Fig. 1(a)** along with the XRD of undoped ZnO in **Fig. 1(b)** (JCPDS 36-1541). The peaks for 1% ammonia addition are shown separately in **Fig. 2(a)** with their deconvolution in **Fig. 2(b)**. The intense peak of GO indicates that the reduction of GO to rGO is in the nascent state for 1% ammonia.

The average crystallite size was close to 15 nm as shown below. Extra peaks other than ZnO and GO were found to be existing due to complex centers containing nitrogen substituting oxygen and Zn interstitial atoms (Zn-No). They act as intrinsic defects responsible for phononic indirect optical transitions as revealed below [30].

Increasing the percentage of NH<sub>3</sub> which acts as the reducing agent of GO has caused an increased crystallinity as observed from the peaks with higher intensity. The

maximum difference is observed between 1 and 2% doping.

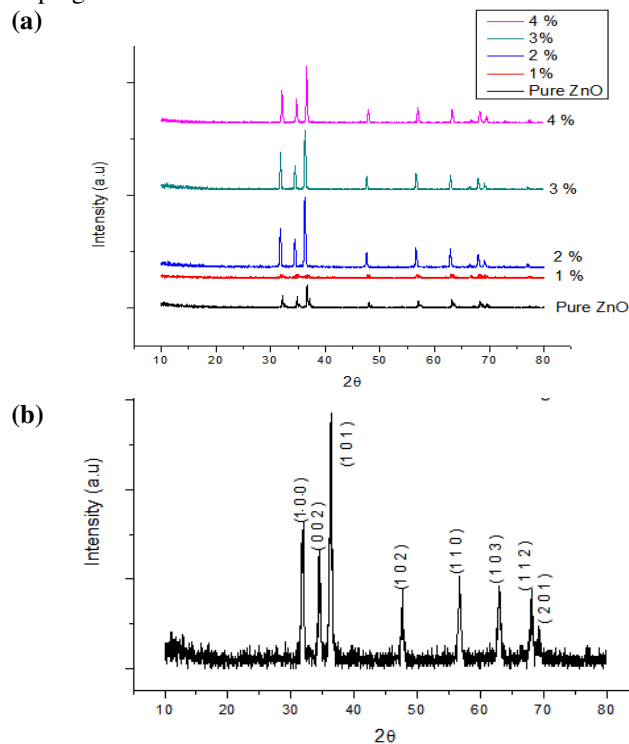


**Fig. 1.** XRD of GO-doped ZnO at different ammonia doping concentrations and pristine ZnO and (b) XRD of undoped ZnO synthesized (Reprinted under CC BY License from Mater Sci Res India 13, 07(2016). Copyright 2016 Oriental Scientific Publishing Company [20].

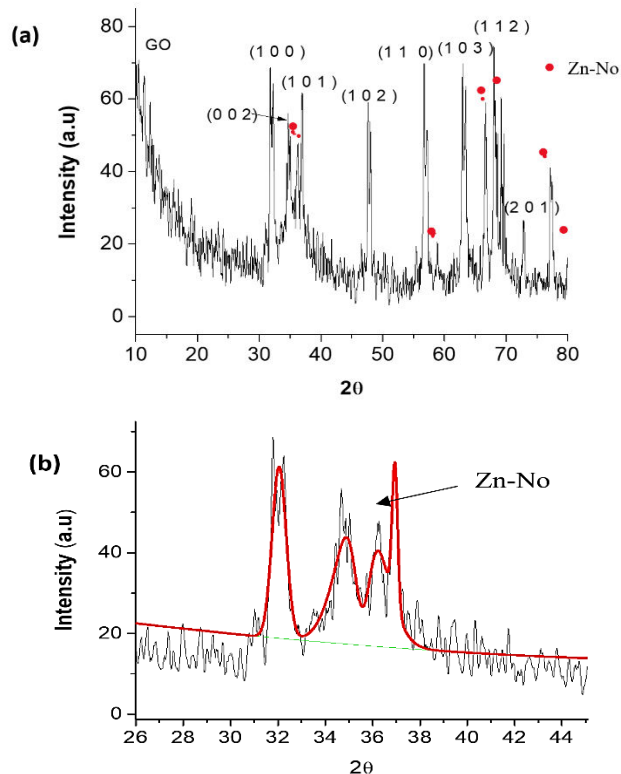


**Fig. 2.** (a) XRD of GO-doped ZnO at 1% ammonia doping concentration (b) Gaussian fit of XRD of ZnO at 1% ammonia doping concentration.

**Table 1.** Parameters obtained from Gaussian Fit find the crystallite size.

2θ (degrees)	36.9	36.2	35.5	32.0
β (degree)	0.23	1	1.79	0.68
D (nm)	38	10	5	15

We observed a slight decrease in intensity with an increase in ammonia concentration from 2 % to 4 %. The peaks between 30° to 40° which are characteristic of ZnO were found to be broadened at the base and sharpened upwards. The particle size from Scherer's formula  $D = \frac{k\lambda}{\beta \cos\theta}$  came as 5nm, 15nm, and 38nm corresponding to the 2θ values of, 35.5°, 32.0° and 36.9° respectively (Table 1), where D is the crystallite size, λ is the wavelength of the X-Ray (1.54 Å), β is the FWHM and θ is half of the Bragg angle. It can be inferred from getting intensity distribution of peaks (JCPDS 36-1541) and crystallite size distribution, that although nucleation of crystallites takes place in a preferential crystallographic orientation, nanoparticles are formed at the base. The peak at 10° is due to GO.

The PL and UV spectra of this sample are shown in Fig. 3(a,b). Deconvolution using Gaussian fits was done of the PL spectra. In PL, luminescence centers arise due to defects like vacancies and interstitials giving different peaks. There are tetrahedral and octahedral sites in the wurtzite structure of ZnO. Oxygen ions are preferentially found in the octahedral sites and oxygen vacancies are also predominant in ZnO compared to Zn<sup>+2</sup> interstitials due to lower energy [31].

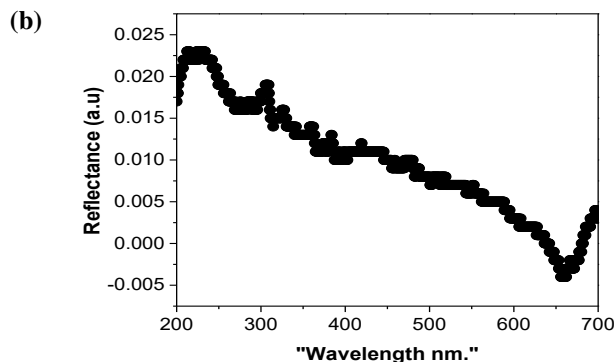
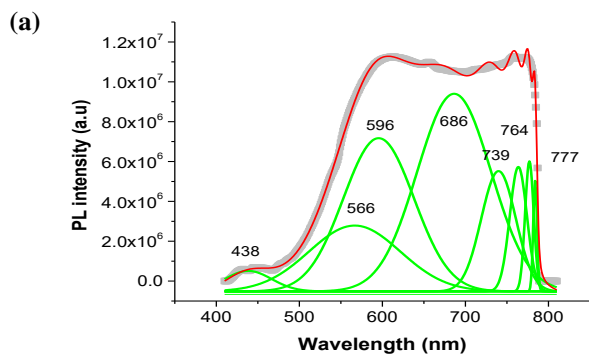


**Fig. 3.** (a) Photoluminescence and (b) UV spectra of 1% NH<sub>3</sub>-GO doped ZnO.

The emission peaks are mainly due to band-to-band excitons' transition or by the transition of electrons from the level of the ionized oxygen vacancies to the valence band. The spectrum has a small violet-blue band at 438 nm, primarily caused by surface imperfections. This small intensity peak is due to a radiative transition between the electron in the conduction band edge and oxygen vacancies (Vo). Two broad green emission bands between 500 – 600nm were observed which is due to the radiative recombination of an electron from the conduction band edge to the deep-level holes. The broadness of the peak is indicative of the fact that phonon-assisted non-radiative transitions are also present. Such non-radiative recombination takes place via levels within the band gap of the semiconductors. The two broad green peaks from 500-600 nm are due to ionized oxygen vacancies (Vo+). The optical centers related to impurities including intrinsic defects are commonly detected in the wavelength range of 450–650 nm. Strong emission bands in the visible range at 500 - 600 nm are formed by the electronic transition in the defect levels for ZnO. Oxygen vacancies are responsible to produce green emissions [32,33].

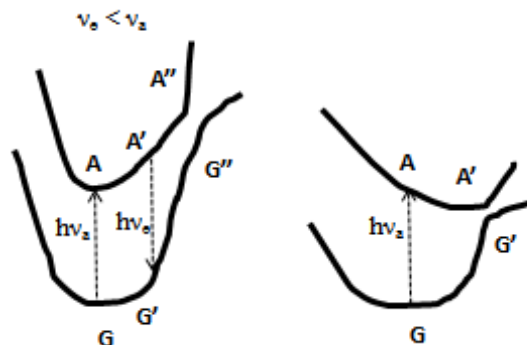


**Fig 4.** Changes in Luminescence due to vibrations and defects.

The lifetime of an excited state is 10<sup>-8</sup> s whereas the frequencies of lattice vibrations are 10<sup>-13</sup> s. Thus, an electron excited to the next vibrational level may not be at the equilibrium (lowest energy) state and may move to equilibrium by non-radiative phonon emission giving a

lower luminescence frequency or higher wavelengths. A radiation-less transition is also possible with heat dissipation decreasing the luminescence spectra as shown in **Fig. 4** where G corresponds to the ground state and A the excited state due to lattice defects.

The UV-vis reflectance spectrum is shown in **Fig. 3(b)**. The band gap energy of nanomaterials may be calculated by Kubelka–Munk equation (**eq 1, 2**).

$$\alpha = F(R) = \frac{(1-R)^2}{(2R)} \quad (1)$$

$$(\alpha h\nu)^{1/n} = A(h\nu - E_g) \quad (2)$$

where  $\alpha$  is the absorption coefficient,  $R$  is reflectance,  $h\nu$  is the incident photon energy;  $A$  is a constant, and  $n$  depends on the type of transition:  $n = 1/2$  and  $2$  for direct and indirect transition, respectively. The Tauc plot showed a reduction in the band gap of ZnO due to indirect transitions (**Fig. 5(a,b)**).

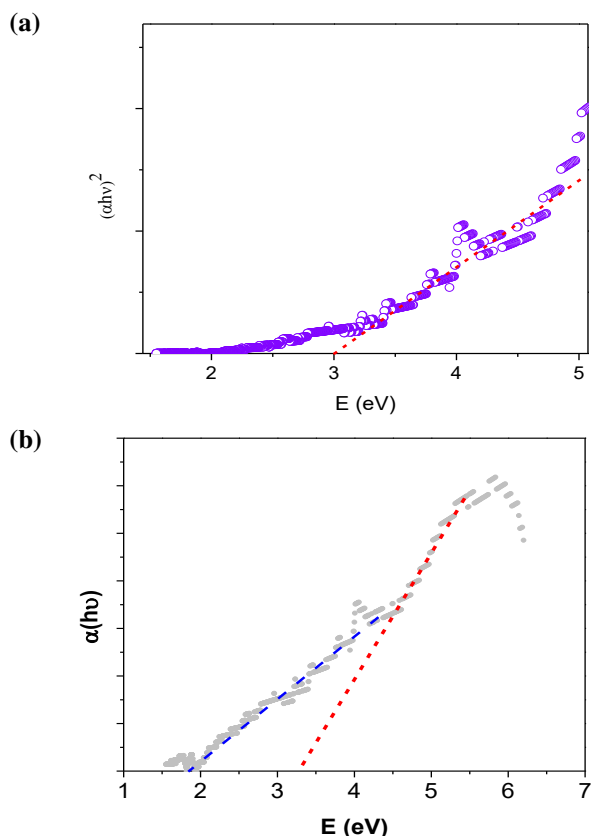


**Fig 5.** Tauc plot of a) rGO–GO direction transition and (b) indirect transitions due to defect states along with direct transition due to ZnO.

The absorption coefficient  $\alpha$  is related to the optical energy band gap ( $E_g$ ) for high photon energies [34, 35]. For direct transitions between conduction and valence bands, it is considered that there is no change in the electron wave vector, and the absorption coefficient for  $\alpha$  ( $E = h\nu$ ) for direct transitions can be expressed as **Eq 3**

$$\alpha_{dir}(h\nu < E_g) = 0 \text{ and } \alpha_{dir}(h\nu \geq E_g) = A(h\nu - E_g)^{1/2} \quad (3)$$

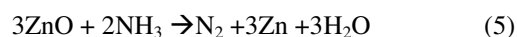
where  $A$  is the constant for direct transition. The linear dependence of  $\alpha(h\nu)^2$  with  $h\nu$ , therefore, indicates direct transition with the determination of  $E_g$  possible using a linear fit [36–38]. Having a long tail is a sign of indirectness which was found in all the cases. It is indicative of the fact that a fraction of indirectness is present in direct transitions. The absorption coefficient for indirect transitions can be expressed as (**eq 4**)

$$\alpha_{ind}(E < E_g) = 0 \text{ and } \alpha_{ind}(E \geq E_g) \propto (E \pm \hbar\Omega - E_g)^n \quad (4)$$

where  $n = 2$  and  $\hbar\Omega$  denotes a phonon being emitted ( $+\hbar\Omega$ ) or absorbed ( $-\hbar\Omega$ ). The equation shows that deviation from linearity is related to indirectness as the order index changes from  $1/2$  to  $2$  and can be used to find the indirect band gap of 1.9 eV as shown in **Fig. 5(b)** in a plot of  $\alpha(h\nu)$  vs  $E$  (eV) [39].

The direct band gap of 3.3 eV is due to ZnO. The indirectness has been induced due to doping, causing non-radiative transition as also observed from the broad peaks in the PL studies. The difference between the two i.e., 1.4 eV is due to phononic modes and is equal to  $\hbar\Omega$  (phonon absorption). The phonon frequency is then estimated to be  $2\pi$  (0.34) femto Hz. which is about  $2\pi$  (1100)  $\text{cm}^{-1}$ . These lattice vibrations cause a reduction in the band gap.

As an increased amount of rGO due to an increase in ammonia concentration has caused better crystallization of the ZnO particles. The indirectness is also expected to get reduced. Due to surface defects like the surface oxygen sites in GO can form OH... N and O...HN hydrogen bonds with  $\text{NH}_3$  and enhance charge transfer between them [40]. These observations are indicative of the fact that. The rGO concentration should be below 2% to get good photocatalytic properties. However, for photoconductive properties a percentage more than 2% of ammonia is beneficial. The reaction kinetics between ZnO and  $\text{NH}_3$  as shown below (**Eq 5**) involves the generation of Zn atoms which go to the interstitial positions and  $\text{N}_2$  which substitutes the oxygen atoms forming Zn-No intrinsic defects as mentioned previously



The substitutional, as well as interstitial N doping, create deep electronic trap states improving charge separation and delaying e- h recombination. and also form Oxygen vacancies. Required for efficient photocatalysis [41]. The defects associated with ZnO within the band gap are either donor-type zinc interstitials ( $\text{Zn}_i^{++}$ ;  $\text{Zn}_i^+$ ;  $\text{Zn}_i^*$ ) and oxygen vacancies ( $\text{V}_O^+$ ;  $\text{V}_O^{++}$  and  $\text{V}_O$ ) or acceptor-type zinc vacancies ( $\text{V}_{\text{Zn}}$  “and  $\text{V}_{\text{Zn}}$  ‘).

A representation of the different states and related transitional wavelengths obtained from PL and UV studies are given in **Table 2** and shown pictorially in **Fig. 7**. The zinc interstitials ( $\text{Zn}_i^*$ ) are lattice defects that cause strain and result in peak shifts as observed in the XRD studies. They are 0.22eV below the conduction band (CB) i.e.,

~3.14 eV and the neutral Zn vacancy state is 0.30 eV above VB. They are formed by Frenkel reactions as  $Zn \rightarrow Zn_i^* + V_{Zn}'$ , creating a zinc vacancy as well. These interstitials can undergo further ionizations to form  $Zn_i^{++}$  and  $Zn_i^+$  losing one electron in each step. These extended zinc interstitial states are 0.54 (2.82 eV) to 0.635 (2.72eV) eV below CB. A transition from  $Zn_i^{++}$  state to VB emitting blue radiation (438 nm) is confirmed. The neutral oxygen vacancy state  $V_o$  is usually 0.86 (2.5 eV) eV below CB. The oxygen vacancy state  $V_o^+$ ; can either capture an electron from CB to form a  $V_o$  state from which a transition to VB occurs emitting a green light (~500 nm), or it can form  $V_o^{++}$  by capturing a hole from the VB. The  $V_o^{++}$  state is found 1.16 eV above VB and therefore electron recombination at the  $V_o^{++}$  state leads to the emission of green light of a higher wavelength (~566 nm = 2.19 eV) as found in our case [41].

The new intrinsic defect states formed are made as i, ii, iii, iv, v. The states i and ii emit yellow and red light respectively while the other states iii, iv, and v are phonic states due to strain induced by Zn-No. They are very close in space (like a band) and are responsible for non-radiative transitions. The GO while interacting with  $NH_3$  can lead to the formation of ammonium ions ( $NH_4^+$ ) and can act as an efficient catalyst in reactions of biological significance [42]. Ammonia also enhances the antibacterial properties of ZnO by causing a reduction in  $Zn^{+2}$  ions which explains the less crystallization observed initially due to ammonia inclusion [44].

**Table 2.** The representation of energy states formed due to intrinsic defects in rGO-ZnO nanocomposites.

Wavelength (nm) (from PL)	Position in the Bandgap (in eV)	Identity	Radiation
438	2.82	$Zn_i^{++} \rightarrow VB$	Blue
566	2.19	$V_o^+ \rightarrow V_o^{++} \rightarrow VB$	Green
596	2.08	(i)	Yellow
686	1.80	(ii)	Red
739	1.68	(iii)	Phononic
764	1.62	(iv)	Phononic
777	1.59	(v)	Phononic

**Fig. 7.** Position of the intrinsic defect states in the band gap of ZnO and corresponding radiations. The unit of the numerical values is eV.

## Conclusions

The rGO-doped ZnO showed nucleation of crystallites in a preferential crystallographic orientation. A lower concentration (< 1%) of the reducing agent ammonia creates intrinsic defect states causing nonradiative optical transitions. The crystallite growth got enhanced with an increase in ammonia concentration. Effects of crystal defect were evident from the PL spectra. The direct band gap of 3.3 eV for the ZnO got lowered in the rGO/ZnO composite and the formation of  $V_o$  took place. Hence

higher photocatalytic activity can be inferred from these materials. Several other defect states were identified to be arising with radiative or non-radiative transitions. The research shows the possibilities of improving and tuning the performance of rGO/ZnO for photocatalytic and other Opto-chemical applications.

## Acknowledgments

The authors would like to thank the integrated master's students of the dept. of nanoscience and technology, the Central University of Jharkhand for their help.

## Conflict of Interest

The authors declare no conflict of interest between them. A preprint version of the manuscript is available [45].

**Keywords:** ZnO, dopants, crystallite size, rGO, ammonia

## References

- H. Beitollahi, S. Tajik, F. G. Nejad, M. Safaei, Recent advances in ZnO nanostructure-based electrochemical sensors and biosensors. *J. Mater. Chem. B*, **2020**, 8, 5826-5844.
- R. S. Rai, V. Bajpai, Recent advances in ZnO nanostructures and their future perspective. *Adv Nano Res.*, **2021**, 11 (1), 37-54.
- G. Kaur, A. Mitra, K.L. Yadav. Pulsed laser deposited Al-doped ZnO thin films for optical applications, *Progress in Natural Science: Materials International*, 25 12–21 (2015).
- M. Akhtar, H. Alhadlaq, A. Alshamsan, A. et al. Aluminum doping tunes band gap energy level as well as oxidative stress-mediated cytotoxicity of ZnO nanoparticles in MCF-7 cells. *Sci Rep.*, 5, 13876 (2015).
- M.M. Khan, S. Kumar, M.N. Khan, M. Ahamed, A. S. Al Dwayyan. Microstructure and blueshift in optical band gap of nanocrystalline  $Al_xZn_{1-x}O$  thin films., *J. Lumine*, 155, 275-281 (2014).
- Soltani, S.; Khanian, N.; Shean Yaw Choong, T.; Asim, N.; Zhao, Y. Microwave- assisted hydrothermal synthesis of sulfonated TiO2-GO core-shell solid spheres as heterogeneous esterification mesoporous catalyst for biodiesel production. *Energy Convers. Manage.*, **2021**, 238, 114165.
- Xi, J.; Huang, J.; Wang, D.; Wen, L.; Hao, J.; He, B.; Chen, J.; Bai, Z. W. Probing Activity Enhancement of Photothermal Catalyst under Near-Infrared Irradiation. *J. Phys. Chem. Lett.*, **2021**, 12, 3443-3448.
- Jo, J.; Yoon, J.; Lee, T.; Cho, H. Y.; Lee, J. Y.; Choi, J. W. H2O2 biosensor consisted of hemoglobin-DNA conjugate on nanoporous gold thin film electrode with electrochemical signal enhancement. *Nano Converg.*, **2019**, 6, 1–8.
- Yek, S. M. G.; Azarifar, D.; Nasrollahzadeh, M.; Bagherzadeh, M.; Shokouhimehr, M. Heterogenized Cu(II) complex of 5-aminotetrazole immobilized on graphene oxide nanosheets as an efficient catalyst for treating environmental contaminants. *Sep. Purif. Technol.*, **2020**, 247, 116952.
- Zain Ul Abideen, Jae-Hun Kim, Ali Mirzaei, Hyoun Woo Kim, Sang Sub Kim, Sensing behavior to ppm-level gases and synergistic sensing mechanism in metal-functionalized rGO-loaded ZnO nanofibers, *Sensors and Actuators B: Chemical*, **2018**, 255, 1884-1896
- Rajitha, Kamalon, Kikkeri Narasimha Shetty Mohana, Mahesh Bhaskar Hegde, Saurav Ramesh Nayak, and Ningappa Kumara Swamy. "Fabrication of ZnO/rGO and ZnO/MWCNT nanohybrids to reinforce the anticorrosion performance of polyurethane coating." *FlatChem.*, **2020**, 24, 100208.
- Elavarasan, N., S. Vignesh, M. Srinivasan, G. Venkatesh, G. Palanisamy, P. Ramasamy, Baskaran Palanivel et al. "Synergistic S-Scheme mechanism insights of g-C3N4 and rGO combined ZnO-Ag heterostructure nanocomposite for efficient photocatalytic and anticancer activities." *Journal of Alloys and Compounds*, **2022**, 906, 164255.

13. Kang, Wang, Xu Jimeng, and Wang Xitao; The effects of ZnO morphology on photocatalytic efficiency of ZnO/RGO nanocomposites. *Applied Surface Science*, **2016**, 360, 270-275.
14. Sen, Sovandeb, and Susmita Kundu; Reduced graphene oxide (rGO) decorated ZnO-SnO<sub>2</sub>: A ternary nanocomposite towards improved low concentration VOC sensing performance. *Journal of Alloys and Compounds*, **2021**, 881, 160406.
15. Sengunthar, Poornima, Shivangi Patel, Nisha Thankachen, and U. S. Joshi; Core-shell hybrid structured rGO decorated ZnO nanorods synthesized via a facile chemical route with photosensitive properties. *New Journal of Chemistry*, **2021**, 45(40), 18853-18862.
16. Jain, Nikita, Savita Sharma, and Nitin K. Puri. "Investigation of charge transport mechanism in hydrothermally synthesized reduced graphene oxide (rGO) incorporated zinc oxide (ZnO) nanocomposite films." *Journal of Materials Science: Materials in Electronics*, **2021**, 1-17.
17. R. Narzary, P. Phukan and P. P. Sahu, "Efficiency Enhancement of Low-Cost Heterojunction Solar Cell by the Incorporation of Highly Conducting rGO Into ZnO Nanostructure," in *IEEE Transactions on Electron Devices*, vol. 68, no. 7, pp. 3238-3245, July **2021**
18. Fahad A. Alharthi, Amjad Abdullah Alsyahi, Saad G. Alshammari, Hessah A. AL-Abdulkarim, Amal AlFawaz, Ali Alsalmeh Synthesis and Characterization of rGO@ZnO Nanocomposites for Esterification of Acetic Acid, *ACS Omega*, **2022**, 7, 3, 2786–2797
19. U. Chinna Rajesh Jinfeng Wang Stuart Prescott, Takuya Tsuzuki, Diwan S. Rawat; RGO/ZnO Nanocomposite: An Efficient, Sustainable, Heterogeneous, Amphiphilic Catalyst for Synthesis of 3-Substituted Indoles in Water. *ACS Sustainable Chem. Eng.*, **2015**, 3, 1, 9–18.
20. P. Mahapatra, S. Kumari, Simran, S. Sharma, K. Gaurav, N. Kumari, P. Kommu, P. Prabhakar and A.S. Bhattacharyya, Synthesis of Hydroxyapatite and ZnO Nanoparticles via Different Routes and its Comparative Analysis, *Mat. Sci. Res. India* 13 (1), 07-13 (**2016**).
21. A.C. Dhanemozhi, V. Rajeswari, S. Sathyajothi. Materials Today: Proceedings, Green Synthesis of Zinc Oxide Nanoparticle Using Green Tea Leaf Extract for Supercapacitor Application 4(2), 660–667 (**2017**).
22. C. B. Ong, L. Y. Ng, A.W. Mohammad, A review of ZnO nanoparticles as solar photocatalysts: Synthesis, mechanisms and applications, *Renewable and Sustainable Energy Reviews*, 81 536–551 (**2018**).
23. P. Cámara, L. Vaccaro, A. Sciortino, F. Messina, G. Buscarino, S. Agnello, F.M. Gelardi, R. Popescu, R. Schneider, D. Gerthsen, M. Cannas, Synthesis of multi-color luminescent ZnO nanoparticles by ultra-short pulsed laser ablation. *Applied Surface Science*, 506, 144954 (**2020**).
24. N. Huang, Y. Cheng, H. Li, L. Zhao, Z. He., C. Zhao, F. Liu, L. Ding. Selective-detection NO at room temperature on porous ZnO nanostructure by solid-state synthesis method. *Journal of Colloid and Interface Science*, 556, 640–649 (**2019**).
25. J. Puneetha J, K. Nagaraju, G. Nagaraju, A. Rathna, Visible light active ZnO nanostructures prepared by simple co-precipitation method. *Photonics, and Nanostructures - Fundamentals and Applications*, 39, 100781 (**2020**).
26. K. Sakata, K. Minhová Macounová, R. Nebel, P. Krtič. pH dependent ZnO nanostructures synthesized by hydrothermal approach and surface sensitivity of their photoelectrochemical behavior. *SN Applied Sciences*, 2(2), 203 (**2020**).
27. Y. Mao, Y. Li, Y. Zou, X. Shen, L. Zhu, G. Liao. Solvothermal synthesis and photocatalytic properties of ZnO micro/nanostructures. *Ceramics Int.*, 45(2), 1724–1729 (**2019**).
28. K. Davis, R. Yarbrough, M. Froeschle, J. White, H. Rathnayake. Band gap engineered zinc oxide nanostructures via a sol-gel synthesis of solvent driven shape-controlled crystal growth; *RSC Advances*, 9(26), 14638–14648 (**2019**).
29. Navas D, Fuentes S, Castro-Alvarez A, Chavez-Angel E. Review on Sol-Gel Synthesis of Perovskite and Oxide Nanomaterials. *Gels*. **2021**, 7(4):275
30. J. Sann, J. Stehr, A. Hofstaetter, and D. M. Hofmann, Zn interstitial related donors in ammonia-treated ZnO powders, *Phys Rev B.*, 76, 195203, **2007**.
31. Rodnyi, P. A., K. A. Chernenko, and I. D. Venetsev; Mechanisms of ZnO luminescence in the visible spectral region, *Optics and Spectroscopy*, 125 (**2018**): 372-378.
32. A. Khalid et al Synthesis of Boron-Doped Zinc Oxide Nanosheets by Using Phyllanthus Emblica Leaf Extract: A Sustainable Environmental Applications. *Front Chem* (**2022**), 10, 930620
33. A. Khalid et al Enhanced Optical and Antibacterial Activity of Hydrothermally, Synthesized Cobalt-Doped Zinc Oxide Cylindrical Microcrystals. *Materials* (**2021**), 14, 3223
34. P. K. Singh, & D. K. Dwivedi. Influence of composition on structural properties and optical parameters of thermally evaporated Ge<sub>10-x</sub>Se<sub>60</sub>Te<sub>30</sub>In<sub>x</sub> (0 ≤ x ≤ 6) thin films. *Ferroelectrics*, **2018**, 531(1), 72-83.
35. S. Mishra, P. K. Singh, P. Lohia, & D. K. Dwivedi. Thin film preparation and optical properties of Se-Te based chalcogenide glasses for optoelectronic applications. *Glass Physics and Chemistry*, **2020**, 46, 341-349.
36. P. K. Singh, S. K. Tripathi, & D. K. Dwivedi. Effect of thermal annealing on structural and optical properties of In doped Ge-Se-Te chalcogenide thin films. *Materials Science-Poland*, **2019**, 37(4), 554-562.
37. P. K. Singh & D. K. Dwivedi. Effect of annealing on the structural and optical properties of amorphous Ge-Se-Te chalcogenide thin film. *Advanced Science, Engineering and Medicine*, **2018**, 10(7-8), 670-674.
38. P. K. Singh, P. Jaiswal, S. Mishra & D. K. Dwivedi. Investigations of heat treatment on structural and optical properties of Ge<sub>8</sub>Se<sub>60</sub>Te<sub>30</sub>In<sub>2</sub> thin film for optical data storage. *Chalcogenide Letters*, **2018**, 15(5), 255-260.
39. A. R. Zanatta, Revisiting the optical bandgap of semiconductors and the proposal of a unified methodology to its determination. *Scientific Reports*, **2019**, 9, 11225
40. Tang, Shaobin, and Zexing Cao. "Adsorption and dissociation of ammonia on graphene oxides: a first-principles study." *The Journal of Physical Chemistry C* 116, no. 15 (**2012**): 8778-8791.
41. Ida Ritacco, Olga Sacco, Lucia Caporaso, and Matteo Farnesi Camellone DFT Investigation of Substitutional and Interstitial Nitrogen-Doping Effects on a ZnO(100)-TiO<sub>2</sub>(101) Heterojunction, *The Journal of Physical Chemistry C.*, **2022**, 126 (6), 3180-3193
42. Kayacı, Fatma & Vempati, Sessa & Donmez, Inci & Biyikli, Necmi & Uyar, Tamer. Role of zinc interstitials and oxygen vacancies of ZnO in photocatalysis: A bottom-up approach to control defect density. *Nanoscale*. 6 (17), **2014**, 10224-10234.
43. Bing Xue, Xiangmei Liu, Na Liu, Yongxin Li, A simple strategy to prepare graphene oxide modified by ammonia gas catalysts for Knoevenagel condensation, *Res Chem Intermed*, **2018**, 44:1523–1536.
44. Junkang Wu, Yan Chang, Huan Gao, Ran Yu, Impacts of ammonia on zinc oxide nanoparticle toxicity to *Nitrosomonas europaea* 2017 IOP Conf. Ser.: *Earth Environ. Sci.* 64 012114
45. Dash, Ritambhara, and Arnab S. Bhattacharyya. "Synthesis of rGO- ZnO Composite and the Effect of Ammonia." *ECSarXiv*. **2022**.